Impact of α-synuclein fibrillar strains and β-amyloid assemblies on mouse cortical neurons endo-lysosomal logistics

Qiao-Ling Chou, Ania Alik, François Marquier, Ronald Melki, François Treussart, Michel Simonneau

eNeuro

Research Article: New Research | Disorders of the Nervous System

Impact of α-synuclein fibrillar strains and ß-amyloid assemblies on mouse cortical neurons endo-lysosomal logistics

https://doi.org/10.1523/ENEURO.0227-21.2022

Cite as: eNeuro 2022; 10.1523/ENEURO.0227-21.2022

Received: 20 May 2021
Revised: 19 January 2022
Accepted: 25 January 2022

Manuscript Title: Impact of α-synuclein fibrillar strains and ß-amyloid assemblies on mouse cortical neurons endo-lysosomal logistics

Abbreviated Title: Protein assemblies and neurons endo-lysosomal logistics

List all Authors: Qiao-Ling Chou[1], Ania Alik[2], François Marquier[1], Ronald Melki[2], François Treussart[1,*] & Michel Simonneau[1,3,*]

[1] Université Paris-Saclay, ENS Paris-Saclay, CNRS, CentraleSupélec, LuMIn, 91190 Gif-sur-Yvette, France.

[2] Laboratory of Neurodegenerative Diseases, Institut François Jacob (MIRCen), CNRS, CEA, Université Paris-Saclay, 92265 Fontenay-aux-Roses cedex, France.

[3] Département d'Enseignement et de Recherche en Biologie, ENS Paris-Saclay, 91190 Gif-sur-Yvette, France.

* co-senior authors

Author contribution: Q-LC, FT, and MS designed research; Q-LC performed research and analyzed data; AA and RM contributed reagents; FM contributed analytic tools; MS, Q-LC and FT wrote the paper.

Corresponding authors: Correspondence should be addressed to François Treussart (francois.treussart@ens-paris-saclay.fr) or Michel Simonneau (michel.simonneau926@gmail.com)

Number of figures: 8 main + 8 extended figures

Number of tables: 0

Number of words:

Abstract: 257

Significant statement: 115

Introduction: 416

Discussion: 1187

Acknowledgements

This work was supported by the Joint Program on Neurodegenerative Disease Research and Agence National de la Recherche (contract TransPathND ANR-17-JPCD-0002) to M.S. and R.M.; Fondation pour la Recherche Médicale (contract ALZ201912009776) to R.M.; Q.L.C. was supported by a PhD scholarship from Taiwan Ministry for Education and University Paris-Saclay and JPND TransPathND (ANR-17-JPCD-0002). .

Conflicts of Interest: Authors report no conflict of interest

Funding sources: Joint Program on Neurodegenerative Disease Research and Agence National de la Recherche (contract TransPathND ANR-17-JPCD-0002); Fondation pour la Recherche Médicale (contract ALZ201912009776) ; PhD scholarship from Taiwan Ministry for Education and University Paris-Saclay.

Abstract

Endosomal transport and positioning cooperate in the establishment of neuronal compartment architecture, dynamics and function, contributing to neuronal intracellular logistics. Furthermore, dysfunction of endo-lysosomal has been identified as a common mechanism in neurodegenerative diseases. Here, we analyzed endo-lysosomal transport when α-synuclein (α-syn) fibrillar polymorphs, ß-amyloid (Aß) fibrils and oligomers were externally applied on primary cultures of mouse cortical neurons. To measure this transport, we used a simple readout based on the spontaneous endocytosis in cultured neurons of fluorescent nanodiamonds, a perfectly stable nano-emitter, and the subsequent automatic extraction and quantification of their directed motions at high-throughput. α-syn fibrillar polymorphs, Aß fibrils and oligomers induce a two-fold decrease of the fraction of nanodiamonds transported along microtubules, while only slightly reducing their interaction with cortical neurons. This important decrease in moving endosomes is expected to have a huge impact on neuronal homeostasis. We next assessed lysosomes dynamics, using Lysotracker. Neurons exposure to Aß oligomers led to an increase in the number of lysosomes, a decrease in the fraction of moving lysosome and an increase in their size, reminiscent of that found in APP transgenic model of Alzheimer's disease. We then analyzed the effect of α-syn fibrillar polymorphs, Aß fibrils and oligomers on endosomal and lysosomal transport and quantified directed transport of those assemblies within cortical neurons. We report different impacts on endosomal and lysosomal transport parameters and differences in the trajectory lengths of cargoes loaded with pathogenic protein assemblies. Our results suggest that intraneuronal pathogenic protein aggregates internalization and transport may represent a target for novel neuroprotective therapeutic strategies.

Significance Statement

Neurodegenerative diseases (NDs) are characterized by the deposition of protein aggregates. These proteins exert a broad range of neuronal toxicity. Defects in endo-lysosomal traffic are increasingly viewed as key pathological features of NDs, likely contributing to synaptic dysfunction and ultimately neuronal death. Here we measured by fast fluorescence videomicroscopy the endosomal and lysosomal dynamics in the branches of primary culture of mouse cortical neurons after externally applying α-syn fibrillar polymorphs (fibrils and ribbons) and Aß assemblies (oligomers and fibrils). We provide significant insight into the differential effects of these pathogenic protein assemblies on endosomal and lysosomal transport, and also reveal distinct transport characteristics of the compartments loaded with these protein assemblies compared to endosome ones.

Introduction

Impairment of axonal transport has recently emerged as a factor shared by several neurodegenerative disorders (Millecamps and Julien, 2013; Morfini et al., 2009). Early impact on intraneuronal transport has been thus proposed as a phenotypic trait common to neurodegenerative diseases such as Alzheimer's, Huntington's and Parkinson's Disease (Stokin et al., 2005; Saudou and Humbert, 2016; Volpicelli-Daley et al., 2014). There is compelling evidence that abnormal protein accumulation in the brain is a key pathophysiological mechanism underlying the neurotoxicity observed in these age-related disorders (Golde et al., 203; Soto et al., 2018). Selective aggregation of misfolded proteins is a hallmark of these neurodegenerative diseases (Saez-Atienzar & Masliah, 2020). An important level of complexity is due to

93 the fact that different species of the same molecules, such as oligomers and fibrils,
94 contribute to a whole spectrum of toxicities (Alam et al., 2017).
95 Few studies have compared, within the same neurons, fibrillary and oligomeric α-
96 synuclein (α-syn) and ß-amyloid (Aß) which are known to be involved in Parkinson
97 and Alzheimer's diseases respectively. Brahic et al., 2016, demonstrated for instance
98 that α-syn, $Aß_{42}$ and HTTExon1 fibrils are transported anterogradely and retrogradely
99 in mice primary neurons grown in microfluidic chambers with different efficiencies in
100 axons. Here, we thoroughly quantified the impact of two α-syn fibrillar polymorphs
101 namely fibrils (α-synF) and ribbons (α-synR), $Aß_{42}$ fibrils (AßF) and oligomers (AßO)
102 on endosomal and lysosomal transports in primary cultures of mouse neurons. To
103 measure this transport and investigate finely its parameters, we relied on our
104 previously established method (Haziza et al., 2017), in which we let perfectly stable
105 and non-toxic fluorescent nanodiamonds (FND) being spontaneously internalized by
106 neurons in endosomes, then follow their displacement by fast video-microscopy and
107 finally apply to the videos our analysis pipeline to extract and analyze single particle
108 trajectories automatically. Using fluorescently-labelled α-syn and Aß assemblies, we
109 conducted the same investigations on their own intraneuronal transport.

110 Our data allow to address three complementary questions: (i) do α-synF, α-synR,
111 AßF and AßO influence the fraction of cargoes moving along the microtubules; (ii) do
112 they impact the dynamics of intracellular endosomal and lysosomal transport.

113 We show here that all pathogenic proteins assemblies reduce the fraction of
114 endosomes moving along microtubules and impact some of their transport
115 parameters. Furthermore, lysosomes properties (number, fraction of lysosomes
116 moving and transport parameters) are also affected by AßO. Finally, our data indicate
117 that cargoes loaded with α-synF, α-synR, AßF or AßO are transported differently

from endosomes, considered as control cargoes, which suggests distinct molecular characteristics of cargo-motor assemblies.

Material and Methods

Production of α-syn fibrillar assemblies, Aß fibrils and oligomers

The expression and purification of human WT α-syn was performed as previously described (Ghee et al., 2005). Pure WT α-syn was incubated in buffer A to obtain the fibrillar polymorph ‘‘fibrils’’ α-synF (50 mM Tris-HCl at pH 7.5, 150 mM KCl) and in buffer B for ‘‘ribbons’’ α-synR (5 mM Tris-HCl at pH 7.5) at 37°C under continuous shaking in an Eppendorf Thermomixer (Hamburg, Germany) set at 600 rotations per minute (rpm) for 4–7 days (Bousset et al., 2013). The fibrillar α-syn polymorphs were centrifuged twice at 15,000 *g* for 10 min and resuspended twice in phosphate-buffered saline (PBS) at 1,446 g/L prior to labeling with ATTO 488 NHS-ester (#AD 488-3, Atto-Tec, Siegen, Germany) fluorophore following the manufacturer’s instructions using a protein/dye ratio of 1:2. The labeling reactions were arrested by addition of 1 mM Tris (pH 7.5). The unreacted fluorophore was removed by a final cycle of two centrifugations at 15,000 *g* for 10 min and resuspensions of the pellets in PBS. This labeling protocol typically yields ≥ 1 ATTO molecule incorporated per α-syn monomer on average as previously demonstrated (Shrivastava et al., 2015). The assemblies were examined by transmission electron microscopy after adsorption on 200 mesh carbon-coated electron microscopy grids and negative stained with 1% uranyl acetate before and after fragmentation using a JEOL 1400 electron microscope (JEOL, Tokyo, Japan).

The expression and purification of Met-Aß 1-42 was performed as described (Walsh et al., 2009). Aß was assembled in PBS, at 4°C or 37°C without shaking for 2 or 24 h to obtain oligomers AßO or fibrils AßF, respectively. The two kinds of assemblies

were labeled with ATTO 488 NHS-ester at a protein/dye ratio of 1:2. The labeling reactions were arrested by addition of 1 mM Tris at pH 7.5. For fibrillar Aß, the unreacted fluorophore was removed by two cycles of centrifugation and resuspension of the pelleted fibrils in PBS as described for α-syn. For oligomeric Aß, the oligomers were separated from the monomeric and fibrillar forms of the protein by size exclusion chromatography on a Superose 6 HR10/300 column (GE Healthcare, Life Sciences, Wauwatosa, WI, USA) equilibrated in PBS pH 7.4 at a flow rate of 0.5 mL/min. Elution was monitored by measuring absorbance at 280 nm wavelength. The Superose 6 column was calibrated with Dextran blue (over 2200 kDa), (670 kDa), β -amylase (200 kDa), BSA (66 kDa), and carbonic anhydrase (29 kDa) standards (Sigma-Aldrich).

Primary mouse cortical neuron cultures

We used commercial primary mouse cortical neurons (ref. Gibco A15586, ThermoFisher) because the provider quality check guarantees a purity of 98% of neurons. The cells were grown on high optical quality glass coverslips (high-precision 170±5 µm thick, 18 mm diameter, ref. 0117580, Marienfeld GmbH, Germany). The coverslips are first cleaned with 70% ethanol, rinsed with water for injection (ref. A128730, ThermoFisher Inc., USA) and exposed during 1 h to UV light. They were then coated with 0.1 mg/ml poly-L-ornithine (ref. P3655, Sigma-Aldrich Merck KGaA, Germany) and placed for 2 h in an incubator set at 37°C, then rinsed twice with water and let dry at biological hood for one hour. We plated an amount of $6x10^5$ primary mouse cortical neurons (ref. Gibco A15586, ThermoFisher) on each coated coverslip, which was then put at the bottom of a 6-wells plate, each well-being finally filled with 3 mL of neurobasal phenol red-free medium (ref. 12348017, ThermoFisher) containing 0.5 mM GlutaMax (ref. 35050061 ThermoFisher), 2% B-27 (ref. 17504044,

ThermoFisher) and 1% PenStrep (ref. 15070063, ThermoFisher). The 6-well plate was then placed in an incubator at 37 °C and 5% CO_2. Half of the volume of the medium was replaced with fresh medium 24 h after plating. We made the subsequent medium changes every 3 days to reduce glutamate toxicity. Neurons were grown until 21 days in culture.

Exposure of mouse cortical neurons to α-syn fibrillar assemblies, Aß fibrils or oligomers

In all the measurements dealing with (1) the impact of pathogenic protein assemblies on endosomal-lysosomal transport, (2) their colocalization with FND-labelled compartment or lysosomes, or (3) the tracking of their intraneuronal transport by fluorescence videomicroscopy, cortical neurons were incubated with either 0.2 μM ATTO 488-labeled α-synF or R, or 1 μM ATTO 488-labeled AßF or AßO.

α-synF or R were added at 24 h, 48 h, or 72 h before observations, while the addition time was either 24 h or 48 h for ATTO 488-labeled AßF or AßO. The video acquisitions of all the experiments were performed at DIC21.

Washing protocol to test the protein assemblies interaction with the neuron membrane

The coverslip with the culture attached to them, were extracted from the well and flushed with PBS first and then twice with culture medium, before FND internalization was carried out following the procedure described in the next paragraph.

Intraneuronal transport cargo labeling

To evaluate the endosomal transport parameters, we relied on our fluorescent nanodiamond assay (Haziza *et al.* 2017). We used commercially available sized 35 nm FND (brFND-35, FND Biotech, Taiwan). Each NP contains an average of 15

nitrogen-vacancy emitters displaying a peak emission wavelength around 700 nm and a full-width at half-maximum of ≈100 nm. This far-red emission allows also to investigate the colocalization of green-emitting ATTO 488-labelled neurodegenerative-disease related species with FND-labeled cargos. FND were internalized in cortical neurons just before the transport analysis, at DIC21. Each culture coverslip was removed from the 6-well plate containing maintaining medium and put in contact with 400 µL of fresh culture medium to which we added 2 µl of stock solution of FNDs (1 mg/mL), reaching a final FND concentration of 5 µg/mL. After 10 mins incubation, the extra FND-containing medium was absorbed by a wiper sheet and the coverslip was placed back to the dish containing the old maintaining medium. The culture was then placed back during 20 mins in the incubator before the video acquisition.

To measure lysosomal transport or investigate the colocalization of neurodegenerative disease-related species with lysosomes, cortical neurons were stained at DIC21, just before the observation, with LysoTracker Deep Red (ref. L12492, ThermoFisher) or Magic Red Cathepsin B substrate (ref. ICT937, Bio-Rad). These dye molecules have an emission spectrum within the similar range than the one of FND. The coverslip was removed from maintaining medium and incubated with prewarmed (37°C) culture medium containing 50 nM LysoTracker or Magic Red (1:20 dilution) for 1 h. The probe-containing medium was replaced with the old maintaining medium and followed by video acquisition.

Pseudo-total internal reflection (TIRF) live-cell videomicroscopy

Pseudo-TIRF illumination was implemented on an inverted microscope (Eclipse Ti-E, Nikon, Japan) as described in details in (Haziza et al. 2017). The whole microscope is enclosed in a cage incubator (Okolab, Italy) to maintain temperature at 37°C. For

the intraneuronal transport recording, each coverslip supporting the neuron culture is mounted at the bottom a Ludin chamber (type 1, Life Imaging Service, Switzerland), installed inside the environmental chamber (in which 5% partial CO_2 pressure and 100% hydrometry is maintained) having a hole at its bottom allowing direct optical access of the microscope objective to the coverslip. We used a ×100 magnification and 1.49 numerical aperture immersion oil objective (CFI Apo TIRF ×100 Oil, Nikon), compatible with differential inference contrast (DIC) mode. Field of views of interest of the neuron cultures were selected in white-light illumination DIC mode. Two continuous-wave lasers are coupled to the microscope and fluorescence was recorded on a cooled EMCCD array detector (DU-885K-CS0, Andor Technologies, UK) of 1004×1002 pixels, with 80 nm pixel size in the sample plane. Two-minutes duration videos were acquired at 20 full frame/s rate large enough to be able to detect short pausing duration in cargoes displacements. EMCCD parameters were selected to provide the largest signal-to-background ratio for FND label tracking at the selected frame rate, leading to EM gain of 90, preamplification gain ×3.8, and digitalization speed of 35 MHz. FNDs and Lysotracker fluorophore were excited with a diode-pumped solid-state laser at a wavelength of 561 nm (SLIM-561-100, Oxxius S.A., France), while ATTO 488 dye was excited with a laser diode emitting at a wavelength of 488 nm (LBX-488-200-CSB-PP, Oxxius S.A). Each excitation laser power was adjusted so that the detection dynamic range of all channels was identical for the above mentioned fixed EMCCD settings. This leads to 561 nm laser excitation power of 60 mW for FND, 200 µW for LysoTracker and 1 mW for Magic Red, and to 488 nm laser excitation power of 200 µW for ATTO 488 dye.

To perform two-color acquisitions and record simultaneously FND (or LysoTracker) and ATTO 488 we combined the two laser beams with a dual-band dichroic filter (ref.

Di01-R488/561, Semrock, USA), and placed a dual imaging system (W-VIEW GEMINI, Hamamatsu, Japan) in front of the EMCCD array detector (DU-885K-CS0, Andor Technologies, UK). This system splits half of the detection field of view (FoV) in two color channels with a dichroic beamsplitter (FF560-FDi01, Semrock) and projects each color on half of the array detector, further preceded by bandpass detection filters (red channel: HC697/75, Semrock; green channel: ET525/50, Chroma Corporation, USA). The result is that each frame of the video contains the same rectangular FoV (1004×501 pixels) in green (ATTO 488) and red (FND and LysoTracker) emission range, allowing to identify spots that colocalize dynamically.

Video processing and intraneuronal transport quantification

Two programs written in python were developed to extract quantitative parameters from videos automatically. The first one relies on Trackpy 0.4.2 package (Trackpy 2019), from which it uses two functions: `locate` to identify isolated spots in each fluorescence frame and fit them with gaussians, and `link` which connects the spots between frames to form trajectories using Crocker-Grier algorithm (Crocker & Grier 1996). Transport parameters are then calculated with a second program which first parses each trajectory into “go” and “stop” phases based on the confinement ratio calculation as described in (Haziza et al., 2017). Four main transport parameters are extracted for each trajectory: velocity, which is the average speed of all go phases; run length: average distance traveled during all go phases; pausing time: average duration of the stop phases, and pausing frequency (events/min). In addition to these four main parameters, we also calculated the total length of the trajectory as the sum of all run lengths during go phases.

Lysosomes size estimation

To get an estimate of the lysosome size from the diffraction limited fluorescence images, we considered the LysoTracker spots as the result of the convolution of the microscope point spread function (assimilated to a gaussian of standard deviation, SD, σ_{PSF}) and the lysosome assimilated to a symmetrical gaussian of SD σ_L. The result of this convolution is also a gaussian of SD σ_T, related to σ_L and σ_{PSF} by ${\sigma_T}^2 = {\sigma_{PSF}}^2 + \sigma_L^2$. σ_T is the so-called "`size`" output of the Trackpy `locate` function. The knowledge of σ_T and σ_{PSF} allows the derivation of σ_L. We then defined the lysosome "diameter" d_L as the full width at half maximum of its gaussian approximation, inferred by $d_L = 2\sqrt{2\ln 2}\,\sigma_L$. For the PSF size σ_{PSF} we took the measured value of the smallest FND spot observed in several trajectories with our microscope. This value was σ_{PSF}=112 nm, consistent with the theoretical Airy radius ρ_A=286 nm (diffraction limit at 700 nm maximum emission wavelength for the 1.49 numerical aperture objective used), and the empirical relation $\sigma_{PSF} = \frac{\rho_A}{3}$, giving here an experimental PSF SD of 286/3=95 nm.

Quantification of fluorescence intensity of ATTO 488-labeled α-synF in cortical neuron branches

We quantify the fluorescence intensity from the first frame of the green channel videos, using Fiji Image J software (Schindelin et al, 2012). We first identify from the DIC image some well-separated and mainly straight neuronal branches, that we surround with the region-of-interest (ROI) polygonal selection tool as close as possible to the branch to include all the fluorescence signal, over a length of 30 µm. We then used the `Analyze` function to measure the average intensity counts per pixel in the defined ROI, to which we subtract the average background counts, measured after having moved the ROI in a region without branches.

Data representation and statistical analysis

All bar plots display the ± standard error on the mean of the distribution. Box plots display the median value as the horizontal line within the box whose limits are 25% and 75% percentiles; bottom and top horizontal lines correspond to 10% and 90% percentiles. As all the data compared between two conditions were random and normally distributed but with unequal variance (as tested with a *F*-test), we performed the relevant comparison test which is the non-parametric Wilcoxon Mann-Whitney two-tailed (implemented in Igor Pro 8, Wavemetrics Inc., USA). Stars referred to the following *p*-value significance level: **p*<0.05; ***p*<0.01; ****p*<0.001.

Results

Quantification of intraneuronal transport using fluorescent nanodiamonds

We quantified the intraneuronal transport with our FND tracking assay (Haziza et al., 2017). We first used a simple readout consisting in counting the number of FND detected in field-of-views (FoV) of size 40×80 µm during 2 minutes. We selected each FoV based on the criteria that it contains approximately the same density of neuronal branches, as estimated from differential interference contrast images (Fig. 1). Our incubation protocol was designed to strongly limit any non-specific interactions of FND, like their attachment to the coverslip supporting the culture, and favor their interaction with neuron membranes and their subsequent internalization in endosomes (Haziza et al., 2017). The perfectly stable fluorescence of FND allows to reconstruct the endosome trajectories accurately and identify “go” and “stop” (none or very slow motion) phases (Fig. 1B) in the transport of FND-labelled endosomes along neuronal branches as observed in differential interference contrast microscopy (Fig. 1C).

α-synF and R affect the number of cargos transported along microtubules without major changes in trajectory length

Primary cultures of mouse cortical neurons were incubated at day in culture (DIC) 20 with α-synF or R at a concentration of 0.2 μM for 24 hours. The intraneuronal transport in these cultures was investigated at DIC21.

Both exposures to α-synF or R led to a small decrease (26% for α-synF and 13% for α-synR) in the number of FND (moving or not) present in each FoV, indicating that both fibrillar polymorphs impact the FND binding to neuronal membrane and their transport dynamics within neurons (Fig. 2*A*). Indeed, if we consider the fraction of these FND having a directed motion, corresponding to those being first internalized in endosomes and then taken in charge by molecular motors, we observed that it decreases by 49%, upon exposure of neurons to α-synF and 45% in the case of α-synR (Fig. 2*B*). The unknown mechanism involved in such a large decrease in the number of cargoes transported along microtubules is expected to impair the functions of cortical neurons.

In order to determine if this important reduction of FND moving fraction is related to the binding of the protein assemblies to the neuronal branches membrane, possibly leading to a reduced endocytosis, we tried in the case of α-synF to wash away the aggregates just before the addition of FND (Materials and Methods), but we found that the interaction of the nanodiamonds with neuron did not change in washed-neuron condition compared to unwashed (Fig. 2-1*A*-*C*); in particular, we did not observe differences in the fraction of moving FND. We concomitantly measured the amount of ATTO 488-labelled assemblies along the neuronal branches (as quantified by the dye fluorescence intensity) and could not see any differences before and after

338 washing (Fig. 2-1*D*-*E*), which is in agreement with FND-neuron interaction results,
339 and indicate a strong binding of α-synF to the neuronal membrane.
340 Using our established FND-based intraneuronal transport assay (Haziza et al., 2017)
341 we detected and quantitatively analyzed the alternation of movement and pause
342 phases of intraneuronal cargoes motion. We first measured the length of trajectories
343 (see Material & Methods) for control FND, FND in the presence of either α-synF or α-
344 synR and we did not evidence any major changes (Fig. 2*C*, Fig. 2*D*; decrease of 4%
345 for α-synF and 5% for α-synR).
346 We then measured four parameters: the curvilinear velocity of each moving phase, its
347 run length, the duration of the pauses and the pausing frequency. The velocity
348 (Fig. 2*E*) and run length (Fig. 2*F*) increases (velocity: 31% and 38%; run length: 80%
349 and 100%, for α-synF and R respectively), the pausing time decreases (Fig. 2*G*; 40%
350 decrease for both fibrillar assemblies) while the pausing frequency increases (Fig. 2*H*;
351 19% and 25%, for α-synF and R respectively). These results are summarized in
352 Fig. 2-2A.
353 We next analyzed the same parameters for lysosomes labelled with Lysotracker red,
354 an established marker of lysosomes, with the difference, compared to FND, that all
355 the fluorescent spots, including the static ones, correspond to lysosomes because
356 Lysotracker only become fluorescent once inside lysosomes. α-synR treatment
357 induces a slight but significant decrease (15%) in the number of lysosomes per field-
358 of-view, while α-synF does not (Fig. 3*A*). This result suggests that α-synR reduce the
359 endocytosis. It is consistent with the observed decrease of FND interacting with
360 neuron (Fig. 2*A*) that possibly reveals their reduced uptake. Furthermore, like for
361 endosomes (Fig. 2*B*), α-synF and R induce a 46% and 32% decrease respectively
362 (resp.) in the fraction of lysosomes having a directed motion (Fig. 3*B*). Analysis of

lysosome trajectory lengths indicates a slight decrease (Fig. 3*C*; 9% and 3% for α-synF and R resp.). Example of FoV showing lysosome trajectories in the different conditions are shown in Fig. 3*D*, where the large decrease in the fraction of lysosomes having a directed motion can be clearly seen.

We quantified the same transport parameters for lysosomes than for FND, using the same experimental paradigm. In contrast to what we observed for endosomes transport, exposure of neurons to α-synF did not lead to any changes in lysosomes transport parameters (Fig. 3*E*-*H*). Interestingly however, in cortical neurons exposed to α-synR, we measured a slight increase of 6% in lysosomes velocity (Fig. 3*E*) and larger one of 26% in run length (Fig. 3*F*), no significant change in pausing time (Fig. 3*G*) and a slight increase of 4% in pausing frequency (Fig. 3*H*). These results are summarized in Fig. 2-2B.

Aß assemblies affect the number of cargos transported along microtubules without major changes in trajectory length

We also analyzed the same parameters after DIC20 mouse cortical neurons exposure to either AßF or AßO, for 24 hours, followed by intracellular transport measurement at DIC21. We used the common 1 µM concentration that has been reported to have a biological impact (Marshall et al., 2020). Figure 4*A* shows a slight decrease (3% and 7% for AßF and AßO resp.) of FND interacting with neurons exposed to AßF or AßO, accompanied by a much larger decrease (56% and 29% for AßF and AßO resp.) of the fraction having directed motions (Fig. 4*B*). FND trajectory lengths stay almost the same for AßF (3% decrease) but are reduced by AßO (Fig. 4*C*, Fig. 4*D*; 13% decrease). We also investigated the effect of Aß assemblies at the smaller concentration of 0.2 µM, identical to the one of α-syn assemblies. Even at this lower concentration, we could detect for both AßF and AßO small decreases

388 (19% and 18% for AßF and AßO resp.) in the number of FND per FoV (Fig. 4-1*A*)
389 and in the fraction of FND having a directed motion (Fig. 4-1*B*; 11% and 18% for AßF
390 and AßO respectively). To summarize, as for α-syn assemblies (Fig. 3), the exposure
391 of cortical neurons to Aß assemblies induce important and significant decreases of
392 the endosomal transport.
393 We then measured more precisely the impact of AßF and AßO on endosomal
394 transports parameters. We observed an increase of FND velocity (Fig. 4*E*; 20% and
395 15% for AßF and AßO resp.) and run length (Fig. 4*F*; 5% and 7% for AßF and AßO
396 resp.), a decrease in their pausing time (Fig. 4*G*; 36% and 12% for AßF and AßO
397 resp.) and an increase of the pausing frequency (Fig. 4*H*; 28% and 15% for AßF and
398 AßO resp.), with effects more pronounced for AßF than for AßO. Interestingly, the
399 same trends of changes were also observed at the lower AßF and AßO concentration
400 of 0.2 µM (Fig. 4-1*C*-*F*). Let us finally point out that for AßF, the important changes of
401 some transport parameters overall combine in an only very slight decrease in
402 trajectory length as shown in Fig 4*C*, which makes the detailed quantitative analysis
403 performed all the more useful. These results are summarized in Fig. 2-2A.
404 Regarding the impact of Aß on lysosomal transport, we noticed large differences
405 between the two types of assemblies AßF and AßO. In neurons exposed to AßO, the
406 total number of lysosomes detected in a FoV as compared to controls increased by
407 50% (Fig. 5*A*) while it stayed unchanged in case of exposure to AßF. The intracellular
408 transport measurements we performed showed that the fraction of moving lysosomes
409 decreased by 1.6-fold and 5.7-fold in neurons exposed to AßF and AßO, respectively
410 (Fig. 5B; from 23% for control to 14% for AßF and 4.5% for AßO). Lysosome
411 trajectory lengths were only slightly decreased for AßF (5%) and more significantly
412 reduced for AßO (Fig. 5C and Fig. 5D; 17% decrease) exposure.

413 We also measured lysosome transport parameters in the presence of 1 µM AßF or
414 AßO (Fig. 5E-H). For AßF, we observed almost no change in velocity (Fig. 5E),
415 pausing time (Fig. 5G), and pausing frequency (Fig. 5H). In contrast, exposure to
416 AßO, led to a 1.7-fold increase of the pausing time. The run length decreased
417 significantly for both assemblies (Fig. 5F; with 9% and 13% decrease for AßF and
418 AßO exposure resp.). These results are summarized in Fig. 2-2B.
419 Furthermore, as changes in lysosome size was described in APP mouse transgenic
420 model of Alzheimer's disease (Gowrishankar et al., 2015), we asked if detectable
421 changes in lysosome diameter can be quantified upon 24 or 48 h exposure to 1 µM
422 AßF and AßO. We detected a slight increase (7%) of lysosome diameter upon
423 exposure of neurons to AßF at 24 h that disappears at 48 h. This contrasts with the
424 increase we observed at both time points (11% and 7% at 24 h and 48 h resp.) in
425 neurons exposed to 1 µM AßO (Fig. 5*I-J* and Fig. 5-1*A-C*). The finding that AßO
426 addition triggers an increase in lysosomes number and size and a decrease in
427 lysosome movements is in agreement with previous reports (Gowrishankar et al.,
428 2015; Marshall et al., 2020).
429 Finally, as LysoTracker can also label other acidic compartments than lysosomes, in
430 particular late endosomes, we repeated the transport experiment with Magic Red
431 substrate that reveals by fluorescence the Cathepsin B protease activity, taking place
432 more specifically in lysosomes. We observed that for both α-synF (Fig. 5-2) and AßF
433 (Fig. 5-3) Magic Red-labelled compartments (lysosomes) behaved the same as
434 LysoTracker-labelled ones for all parameters, with in particular a ≈40% decrease of
435 the mobile fraction of Magic Red and LysoTracker-labelled compartment in the
436 presence of the fibrillar assemblies, and similar colocalization data at 24 h, *i.e.* small
437 colocalization of 4-7% for α-synF compared to 40% for AßF. These results indicates

438 that, in our case, LysoTracker and Magic Red labeling largely overlap and that we
439 can rely on LysoTracker puncta density to quantify endocytic activity as we did.
440 These results are summarized in Fig. 2-2C.

441 **Transport of α-syn and Aß assemblies within cortical neurons.**

442 We also assessed α-syn and Aß assemblies transport within cortical neurons while
443 documenting their impact on endosomes and lysosomes dynamics. As ATTO 488
444 dye used to label α-syn and Aß assemblies exhibit no emission spectrum overlap
445 with neither FND nor Lysotracker deep red, we were able to measure simultaneously
446 the transport properties of endosome or lysosome and the assemblies on two-color
447 channels.

448 We first studied α-syn fibrillar assemblies transport (Fig. 6). We found that α-synF
449 and R display directed movements as shown by examples of trajectories in Fig. 6*A*-*B*.
450 We compared these motions to the endosomal transport in the presence of α-syn
451 fibrillar polymorphs. Interestingly, α-syn F and R trajectories are about 29% shorter
452 than those of FND (Fig. 6*C*). We also compared the transport parameters and found
453 smaller velocity (Fig. 6*D*; 5% and 10% for α-synF and α-synR resp.), run length
454 (Fig. 6*E*; 39% and 46% for α-synF and α-synR resp.) and pausing time (Fig. 6*F*; 19%
455 and 21% for α-synF and α-synR resp.) for α-synF and α-synR-loaded cargoes
456 compared to those of FND-containing endosomes. On the contrary, α-synF and R
457 pausing frequencies were larger than those of FND (Fig. 6*G*; 19% and 8% for α-synF
458 and α-synR resp.). The shorter trajectories length and run-length together with the
459 larger pausing frequency, suggest that cargoes loaded with α-synF- and R are
460 transported less efficiently than those containing FND.

461 Similarly, we also investigated ATTO 488-labelled AßF and AßO intraneuronal
462 transport (Fig. 7) at the concentration of 1 µM, as we could not detect their

fluorescence signal at 0.2 µM. Both species exhibit directed transport as shown by examples of trajectories in Fig. 7*A*-*B*. These trajectories are shorter than the ones of FND in the same conditions (Fig. 7*C*), as for α-syn fibrillar assemblies. Regarding the transport parameters, compared to FND, AßF and AßO have slightly larger velocity (Fig. 7*D*; 8% and 12% for AßF and AßO resp.), and a trend towards a shorter run-length (Fig. 7*E*; 7% and 28% for AßF and AßO resp.). As α-syn fibrillar assemblies, AßF and AßO exhibit a much shorter pausing time (Fig. 7*F*; 49% and 53% for AßF and AßO resp.) and a much larger pausing frequency (Fig. 7*G*; 41 and 36% for AßF and AßO resp.). As for α-syn fibrillar assemblies the shorter trajectories length and run-length together with the larger pausing frequency suggest that cargoes loaded with AßF and AßO are transported less efficiently than those containing FND.

Moreover, since differences in AßO and AßF uptake in cultured neurons were recently reported (Vadukul et al., 2020), we also investigated the related aspect of the number of Aß assembly trajectories per field-of-view at 24 h and 48 h time points (Fig. 7-1). We did not observe differences in the number of trajectories 24 h after addition of the assemblies (Fig. 7-1*A*) in agreement with Fig. 4B of (Vadukul *et al.* 2020). However, at 48 h time point, we measured a ≈2.5 lower number of AßO trajectories compared to AßF ones (Fig. 7-1*B*), which differs to uptake results of (Vadukul *et al.* 2020) at 72 h time point, who reported a ≈1.5 times larger amount of internalized AßO compared to AßF(sonicated). Our observations differ from (Vadukul *et al.* 2020), but several reasons may explain this discrepancy: (i) we quantify only the moving fraction of Aß assemblies; (ii) we do not have the 72 h point, and finally (iii) we do not use the exact same AßF.

Finally, we assessed in a quantitative manner the co-localization of α-syn and Aß assemblies with lysosomes, as a function of neuron exposure time at 24 and

48 hours (Fig. 8). While the fraction of α-syn fibrillar assemblies moving within lysosomes increases from ≈4% at 24 h to 12-14% at 72 h (Fig. 8*A*), it reaches already ≈41% at 24 h for Aß fibrils continuing its increase up to ≈51% at 48 h (Fig. 8*B*). AßO moving in or with lysosomes have slightly lower colocalization proportions, however much larger than for α-syn fibrillar assemblies. We repeated these analyses with Magic Red labeling instead of LysoTracker for α-synF (Fig. 8-1*A*) and AßF (Fig. 8-1*B*) at 24 h and achieved similar results, with a ≈40% colocalization fraction of AßF with Magic Red-labelled lysosomes, and only ≈7% for α-synF.

Discussion

In this work, we investigated the generic effects of α-syn fibrillar polymorphs (fibrils and ribbons) and Aß assemblies (oligomers and fibrils) on endosomal and lysosomal movements in mouse cortical neurons. In neurons, early endosomes and lysosomes move using different types of machinery. Also, the former are compartmentalized (dendrites vs. axon) while the latter are not (Winckler et al., 2018). However, due to the high density of the cultures it was not possible to identify unambiguously the compartment (dendrite or axon) in which the traced vesicles moved, and therefore we could not study separately the impact of the protein assemblies on axonal and dendritic endolysosomal transports.

Potential consequences of a decrease in the number of cargos transported at a given time within cortical neuron

The exposure of cortical neurons to α-syn and Aß assemblies led to important reductions (between 32% and 56%) of moving endosomes and lysosomes along neuronal branches (Figs. 1-2). We previously showed that pathogenic α-syn and Aß assemblies bind the plasma membrane with, as a consequence, a redistribution of

512 essential membrane proteins (Renner et al. 2010; Shrivastava et al., 2013;
513 Shrivastava et al., 2015). We further reviewed the physico-pathogenic mechanisms
514 at the origin and resulting from pathogenic proteins assemblies-plasma membrane
515 components interactions (Shrivastava et al., 2017). The reduction we report here
516 might be due to changes in membrane dynamics and endocytosis rate.
517 Exposure of cortical neurons to α-syn and Aß assemblies affected moving FND-
518 containing endosome properties. α-syn fibrillar assemblies increased their velocity by
519 31-38% and run length by 80-100% (Fig. 2*E*-*F*) and decreased their pausing time by
520 40% (Fig. 2*G*) while increasing their pausing frequency to a lesser extend (19-25%,
521 Fig. 2*H*). We observed similar effects but less pronounced for moving FND-
522 containing endosomes when neurons are exposed to AßF or AßO (Fig. 4*E*-*H*). These
523 changes reflect an increase in mobility of moving FND-containing endosomes. Hence,
524 while decreasing the fraction of moving FND-labeled endosomes, α-synF and R or
525 AßF and AßO, increase the overall mobility of the moving ones (Fig. 2-2*A*).
526 A decrease in the number of moving endosomes or lysosomes can affect protein
527 quality control, accompanied by limited elimination of damaged membrane and
528 cytosolic proteins, protein aggregates, and membranous organelles (Winckler et al.,
529 2018). Furthermore, considering that lysosomes and late endosomes act as mRNA
530 translation platforms (Cioni et al., 2019; Liao et al., 2019; Fernandopulle et al., 2021),
531 changes in the number of cargos transported at a given time within a cortical neuron
532 is expected to dramatically impact mRNA translation platform either in dendrites or in
533 axons. In particular, the regulation of protein synthesis and degradation at the
534 neuronal synapse is local and dynamic and modify the synaptic proteome
535 autonomously during plasticity (Giandomenico et al., 2021). Hence, the synaptic
536 function can be impacted if the number of moving lysosomes is affected.

Effect of α-syn and Aß assemblies on lysosomes transport

We observed that α-synF (Fig. 3E-H) and AßF (Fig. 5E-H) barely impact the lysosomal transport parameters as compared to the control. In contrast, α-synR (Fig. 3E-H) and AßO (Fig. 5E-H) induce significant changes of lysosomes transport parameters (Fig. 2-2*B*). Furthermore, the size of lysosomes significantly increased in the presence of AßO (Fig. 5I-J). This set of impairments of lysosomal transport in Alzheimer-related context are in full agreement with previous reports (Gowrishankar et al., 2015; Marshall et al., 2020). Indeed, using a mouse model of Alzheimer's disease, (Gowrishankar et al., 2015) evidenced axonal lysosome accumulations with local impairment in the retrograde axonal transport of lysosome precursors. Similarly, (Marshall et al., 2020) found that misfolded $Aß_{42}$ impacts the endo-lysosomal pathway. They reported impairments in the uptake of proteins that use a dynamin-dependent endosomal mechanism and accumulation of lysosomes.

Intraneuronal transport of neurodegenerative-related molecular species

We were able to quantity the intraneuronal transport parameters for α-syn and Aß pathogenic species (Figs 6-7). We found that cargoes loaded with α-synF and R exhibit a more dynamical transport compared to those containing FND that are characterized by a larger pausing frequency and shorter run-length and pausing time (Fig. 6*D*-*G*). AßF and AßO-containing endosomes exhibit similar characteristics (Fig. 7*D*-*G*) with in addition an increase in velocity, not observed for α-synF and R. These results suggest that similar molecular mechanisms are at play in the transport of the two α-syn fibrillar polymorphs, the AßF and AßO. However, the ≈7-fold larger fraction of AßF and AßO found in moving lysosomes compared to α-syn assemblies (Fig. 8), also indicate differences in the molecular interactions of Aß assemblies with

561 lysosomes. These results suggest either a cellular triage leading to differential
562 transport of α-syn and Aß assemblies.

563 **Potential application in drug discovery assay**

564 We report here the use of a model based on primary mouse cortical neurons where it
565 is possible to identify a robust decrease in the number of vesicles moving
566 intracellularly (Figs. 2*B*, 3*B*, 4*B* and 5*B*), in the order of 30-50%, and up to 5-fold for
567 lysosomes in neurons exposed to AßO (Fig. 5*B*). Such a large decrease is likely to
568 impact the physiology of neurons and it is reasonable to consider that the transport of
569 other cargoes, such as mitochondria and RNA granules, is also affected. This
570 endolysosomal transport impairment endophenotype can be instrumental in
571 generating large-scale drug-discovery campaigns (*i.e.*, $>10^5$ compounds) as used in
572 more complex human cellular models (Park et al., 2021).
573 The cargoes transport blockade within cortical neurons we report could either result
574 from a direct interaction between pathogenic aggregates and the intraneuronal
575 transport machinery or a pathogenic aggregates-mediated transcriptional changes in
576 transport proteins expression (Encalada and Goldstein, 2014, Lee et al., 2014; Guo
577 et al., 2020). Analysis of neuronal immuno-precipitates of α-syn fibrillar assemblies
578 and Aß polymorphs may be instrumental to identify the molecular partners that
579 directly interact with these protein assemblies. A recent postmortem proteomics study
580 identified proteins whose abundance changed at different stages of Alzheimer's
581 disease (Li et al., 2021). At its early stage, differentially expressed proteins of
582 "clathrin-coated endocytic vesicle membrane" (GO: 0030669) and the secretory
583 pathway (R-HSA-432720: "Lysosome Vesicle Biogenesis" and R-HSA-432722: "Golgi
584 Associated Vesicle Biogenesis") classes were over-represented. Comparison of
585 proteome profile changes in our neuronal model with (Li et al., 2021) profiles can be

586 instrumental to identify druggable targets in order to enhance the number of
587 transported cargoes.
588 Finally, we quantified intraneuronal transport of neurodegenerative-linked molecular
589 species (α-syn fibrillar polymorphs, AβF and oligomers) whose transport
590 characteristics are distinct from those of endosomes but for which no molecular
591 characterization is yet available. Furthermore, we observed that all these protein
592 assemblies are transported intracellularly in cortical neurons with very similar
593 quantitative characteristics. We could not detect differences in their transport
594 parameters. Further work will be required to identify a possible common transport
595 mechanism and the identification of specific molecules involved in this transport can
596 allow to selectively inhibit it.
597 These results also need to be considered from the standpoint of the prion-like spread
598 of pathogenic protein particles between neurons (Brundin et al., 2010; Hardy and
599 Revesz, 2012; Jucker and Walker, 2018). Selective inhibition may avoid the spread
600 of these neurotoxic species. Thus, advances in the identification of targets involved in
601 cargoes loaded with pathogenic protein aggregates transport may lead to novel
602 neuroprotective therapeutic avenues.

603 References

604 Alam P, Bousset L, Melki R, Otzen DE (2019) α-synuclein oligomers and fibrils: a
605 spectrum of species, a spectrum of toxicities. J Neurochem 150(5):522-534.
606 Brahic M, Bousset L, Bieri G, Melki R, Gitler AD (2016) Axonal transport and
607 secretion of fibrillar forms of α-synuclein, $A\beta_{42}$ peptide and HTTExon 1. Acta
608 Neuropathol 131(4):539-48.

609 Braak H, Braak E (1991) Neuropathological stageing of Alzheimer-related changes.
610 Acta Neuropathol 82:239-259.

611 Braak H, Del Tredici K, Ru¨b U, de Vos RAI, Jansen Steur ENH, Braak E (2003)
612 Staging of brain pathology related to sporadic Parkinson's disease. Neurobiol Aging
613 24:197-21.

614 Brundin P, Melki R, Kopito R (2010) Prion-like transmission of protein aggregates in
615 neurodegenerative diseases. Nat Rev Mol Cell Biol 11(4):301-7.

616 Cioni JM, Lin JQ, Holtermann AV, Koppers M, Jakobs MAH, Azizi A, Turner-Bridger
617 B, Shigeoka T, Franze K, Harris WA, Holt CE (2019) Late Endosomes Act as mRNA
618 Translation Platforms and Sustain Mitochondria in Axons. Cell 176(1-2):56-72.e15.

619 Crocker JC, Grier DG (1996) Methods of Digital Video Microscopy for Colloidal
620 Studies. J Colloid Interf Sci 179:298–310.

621 Encalada SE, Goldstein LS (2014) Biophysical challenges to axonal transport: motor-
622 cargo deficiencies and neurodegeneration. Annu Rev Biophys 43:141-69

623 Fernandopulle MS, Lippincott-Schwartz J, Ward ME (2021) RNA transport and local
624 translation in neurodevelopmental and neurodegenerative disease. Nat Neurosci
625 24(5):622-632.

626 Ghee M, Melki R, Michot N, Mallet J (2005) PA700, the regulatory complex of the
627 26S proteasome, interferes with alpha-synuclein assembly. FEBS J272:4023–4033.

628 Giandomenico SL, Alvarez-Castelao B, Schuman EM (2021) Proteostatic regulation
629 in neuronal compartments. Trends Neurosci 3:S0166-2236(21)00161-2.

630 Golde TE, Borchelt DR, Giasson BI & Lewis J (2013) Thinking laterally about
631 neurodegenerative proteinopathies. J. Clin. Invest 123:1847–1855.

632 Gowrishankar S, Yuan P, Wu Y, Schrag M, Paradise S, Grutzendler J, De Camilli P,
633 Ferguson SM (2015) Massive accumulation of luminal protease-deficient axonal
634 lysosomes at Alzheimer's disease amyloid plaques. Proc Natl Acad Sci U S A
635 14;112(28):E3699-708.

636 Guo W, Stoklund Dittlau K, Van Den Bosch L (2020) Axonal transport defects and
637 neurodegeneration: Molecular mechanisms and therapeutic implications. Semin Cell
638 Dev Biol 99:133-150.

639 Hardy J, Revesz T (2012) The spread of neurodegenerative disease. N Engl J Med
640 366(22):2126-8.

641 Haziza S, Mohan N, Loe-Mie Y, Lepagnol-Bestel AM, Massou S, Adam MP, Le XL,
642 Viard J, Plancon C, Daudin R, Koebel P, Dorard E, Rose C, Hsieh FJ, Wu CC, Potier
643 B, Herault Y, Sala C, Corvin A, Allinquant B, Chang HC, Treussart F, Simonneau M
644 (2017) Fluorescent nanodiamond tracking reveals intraneuronal transport
645 abnormalities induced by brain-disease-related genetic risk factors. Nat Nanotechnol
646 12(4):322-328.

647 Jucker M, Walker LC (2018) Propagation and spread of pathogenic protein
648 assemblies in neurodegenerative diseases. Nat Neurosci 21(10):1341-1349.

649 Lee WC, Yoshihara M, Littleton JT (2004) Cytoplasmic aggregates trap
650 polyglutamine-containing proteins and block axonal transport in a Drosophila model
651 of Huntington's disease. Proc Natl Acad Sci U S A 101(9):3224-9.

652 Li X, Tsolis KC, Koper MJ, Ronisz A, Ospitalieri S, von Arnim CAF, Vandenberghe R,
653 Tousseyn T, Scheuerle A, Economou A, Carpentier S, Otto M, Thal DR (2021)
654 Sequence of proteome profiles in preclinical and symptomatic Alzheimer's disease.
655 Alzheimers Dement.

Liao YC, Fernandopulle MS, Wang G, Choi H, Hao L, Drerup CM, Patel R, Qamar S, Nixon-Abell J, Shen Y, Meadows W, Vendruscolo M, Knowles TPJ, Nelson M, Czekalska MA, Musteikyte G, Gachechiladze MA, Stephens CA, Pasolli HA, Forrest LR, St George-Hyslop P, Lippincott-Schwartz J, Ward ME (2019) RNA Granules Hitchhike on Lysosomes for Long-Distance Transport, Using Annexin A11 as a Molecular Tether. Cell 19;179(1):147-164.e20.

Marshall KE, Vadukul DM, Staras K, Serpell LC (2020) Misfolded amyloid-beta-42 impairs the endosomal-lysosomal pathway. Cell Mol Life Sci 77(23):5031-5043.

De Matteis MA, Luini A (2011) Mendelian disorders of membrane trafficking. N Engl J Med 8;365(10):927-38.

Millecamps S, Julien JP (2013) Axonal transport deficits and neurodegenerative diseases. Nat Rev Neurosci 14(3):161-76.

Morfini GA, Burns M, Binder LI, Kanaan NM, LaPointe N, Bosco DA, Brown RH, Brown H, Tiwari A, Hayward L, Edgar J, Nave K-A, Garberrn J, Atagi Y, Song Y, Pigino G, Brady ST (2009) Axonal Transport Defects in Neurodegenerative Diseases. J Neurosci 29:12776–12786.

Park J-C, Jang S-Y, Lee D, Lee J, Kang U, Chang H, Kim HJ, Han S-H, Seo J, Choi M, Lee DY, Byun MS, Yi D, Cho K-H, Mook-Jung I (2021) A logical network-based drug-screening platform for Alzheimer's disease representing pathological features of human brain organoids. Nat Commun 12:280.

Peelaerts W, Bousset L, Van der Perren A, Moskalyuk A, Pulizzi R, Giugliano M, Van den Haute C, Melki R, Baekelandt V (2015) α-Synuclein strains cause distinct synucleinopathies after local and systemic administration. Nature 522(7556):340-4.

679 Renner M, Lacor PN, Velasco PT, Xu J, Contractor A, Klein WL, and Triller A (2010)
680 Deleterious effects of amyloid b oligomers acting as an extracellular scaffold for
681 mGluR5. Neuron 66:739–754.Saez-Atienzar S, Masliah E. Cellular senescence and
682 Alzheimer disease: the egg and the chicken scenario. Nat Rev Neurosci 21(8):433-
683 444.

684 Sardana R, Emr SD (2021) Membrane Protein Quality Control Mechanisms in the
685 Endo-Lysosome System. Trends Cell Biol 31:269–283.

686 Saudou F, Humbert S (2016) The Biology of Huntingtin. Neuron 89(5):910-926.

687 Schindelin J, Arganda-Carreras I, Frise E, Kaynig V, Longair M, Pietzsch T, Preibisch
688 S, Rueden C, Saalfeld S, Schmid B, Tinevez J-Y, White DJ, Hartenstein V, Eliceiri K,
689 Tomancak P, Cardona A (2012) Fiji: an open-source platform for biological-image
690 analysis. Nat Methods 9:676–682.

691 Shrivastava AN, Aperia A, Melki R, Triller A. (2017) Physico-Pathologic Mechanisms
692 Involved in Neurodegeneration: Misfolded Protein-Plasma Membrane Interactions.
693 Neuron 95(1):33-50.

694 Shrivastava AN, Bousset L, Renner M, Redeker V, Savistchenko J, Triller A, Melki R.
695 (2020) Differential Membrane Binding and Seeding of Distinct α-Synuclein Fibrillar
696 Polymorphs. Biophys J 118(6):1301-1320.

697 Shrivastava AN, Kowalewski J.M., Renner M., Bousset L, Koulakoff A, Melki R,
698 Giaume C, and Triller A (2013) ß-amyloid and ATP-induced diffusional trapping of
699 astrocyte and neuronal metabotropic glutamate type-5 receptors. Glia 61:1673–1686.

700 Shrivastava AN, Redeker V, Fritz N, Pieri L, Almeida LG, Spolidoro M, Liebmann T,
701 Bousset L, Renner M, Léna C, Aperia A, Melki R, Triller A. (2015) alpha-synuclein

assemblies sequester neuronal alpha3-Na+/K+-ATPase and impair Na+ gradient. EMBO J 34(19):2408-23.

Shrivastava AN, Redeker V, Pieri L, Bousset L, Renner M, Madiona K, Mailhes-Hamon C, Coens A, Buée L, Hantraye P, Triller A, Melki R. (2019) Clustering of Tau fibrils impairs the synaptic composition of α3-Na+/K+-ATPase and AMPA receptors. EMBO J 38(3):e99871.

Soto C, Pritzkow S (2018) Protein misfolding, aggregation, and conformational strains in neurodegenerative diseases. Nat. Neurosci 21:1332–1340.

Stokin GB, Lillo C, Falzone TL, Brusch RG, Rockenstein E, Mount SL, Raman R, Davies P, Masliah E, Williams DS, Goldstein, LS. (2005) Axonopathy and transport deficits early in the pathogenesis of Alzheimer's disease. Science 307:1282–1288.

Trackpy (2019), doi: 10.5281/zenodo.3492186

Valm AM, Cohen S, Legant WR, Melunis J, Hershberg U, Wait E, Cohen AR, Davidson MW, Betzig E, Lippincott-Schwartz J. (2017) Applying systems-level spectral imaging and analysis to reveal the organelle interactome. Nature 546(7656):162-167.

Victoria GS, Zurzolo C. (2017) The spread of prion-like proteins by lysosomes and tunneling nanotubes: Implications for neurodegenerative diseases. J Cell Biol 216(9):2633-2644.

Volpicelli-Daley LA, Gamble KL, Schultheiss CE, Riddle DM, West AB, Lee VM. (2014) Parkinson’s disease Formation of α-synuclein Lewy neurite-like aggregates in axons impedes the transport of distinct endosomes. Mol Biol Cell 25(25):4010-23.

724 Walker LC, Jucker M. (2015) Neurodegenerative diseases: expanding the prion
725 concept. Annu Rev Neurosci 38:87-103.

726 Walsh DM, Thulin E, Minogue AM, Gustavsson N, Pang E, Teplow DB, Linse S
727 (2009) A facile method for expression and purification of the Alzheimer's disease-
728 associated amyloid beta-peptide. FEBS J 276:1266–1281.

729 Winckler B, Faundez V, Maday S, Cai Q, Almeida CG, Zhang H (2018) The
730 Endolysosomal System and Proteostasis: From Development to Degeneration. J
731 Neurosci 38:9364–9374.

732

733 ## Figure Legends

734 **Figure 1.** Recording fluorescent nanodiamond trajectories in mouse cortical neurons
735 at DIC21. ***A***, Schematic representation of the cargoes that are tracked thanks to
736 FND, at different stages after their endocytosis. We previously showed (Haziza et al.,
737 2017) that FND are present in cargos at different stage of their lifetime after
738 endocytosis, as shown by colocalization measurements with specific membrane
739 protein markers: Rab5 for early endosome; Rab7 for late endosome; Rab11 for
740 recycling endosome; Lysotracker for the lysosome. ***B***, Illustration of FND trajectories
741 with go (green) and stop (red) phases. ***C***, Differential interference contrast images of
742 cortical neurons overlapped with 10 representative trajectories. Scale bar: 10 μm.
743
744 **Figure 2**. Effect of α-synF or R on the mobility of endosomes and their transport as
745 measured by tracking FND-containing cargoes in mouse cortical neurons at DIC21.
746 24 h exposure to α-synF or R at 0.2 μM concentration, compared to nothing added
747 control (Ctrl). ***A,*** Number of FNDs detected per field-of-view of 40 μm x 80 μm size
748 during 2 mins of observation. ***B***, Fraction of FNDs-containing cargoes having a
749 directed motion. ***C***, Length of FND trajectories. ***D***, Examples of FND trajectories.
750 Scale bar: 10 μm. ***E-H***, Comparison of four transport parameters: ***E***, curvilinear
751 velocity, ***F***, run length, ***G***, pausing time and ***H***, pausing frequency. The number within
752 each bar represents the total number of FoV (***A***, ***B***) or trajectories (***C***, ***E***-***H***) analyzed
753 from *n*=8 coverslips (four independent cultures). Inset: box-plots representation of the
754 same dataset. See also Figure 2-1 and Fig. 2-2.
755
756 **Figure 3.** Effect of α-synF or α-synR on the mobility of LysoTracker-labelled
757 lysosomes and their transport in mouse cortical neurons at DIC21. 24 h exposure to

758 α-synF or α-synR at 0.2 μM concentration, compared to nothing added control (Ctrl).
759 ***A***, Number of lysosomes detected per field-of-view of 40 x 80 μm size during 2 mins
760 of observation. ***B***, Fraction of lysosomes having a directed motion. ***C***, Length of
761 lysosome trajectories. ***D***, Examples of lysosome trajectories. Scale bar: 10 μm. ***E-H*****,**
762 Comparison of four transport parameters: curvilinear velocity (***E***), run length (***F***),
763 pausing time (***G***) and **H**, pausing frequency (**H**). The number within each bar
764 represents the total number of FoV (***A***, ***B***) or trajectories (***C***, ***E-H***) analyzed from *n*=2
765 coverslips (from one culture). Inset: box-plots representation of the same dataset.
766
767 **Figure 4.** Effect of AßF and AßO on the mobility of endosomes and their transport as
768 measured by tracking FND-containing cargoes in mouse cortical neurons at DIC21.
769 24 h exposure to AßF and AßO at 1 μM concentration, compared to nothing added
770 control (Ctrl). ***A***, Number of FNDs detected per field-of-view of 40 x 80 μm size during
771 2 mins of observation. ***B***, Fraction of FNDs-containing cargoes having a directed
772 motion. ***C***, Length of FND trajectories. ***D***, Examples of FND trajectories. Scale bar:
773 10 μm. ***E-H***, Comparison of four transport parameters: curvilinear velocity (***E***), run
774 length (***F***), pausing time (***G***) and pausing frequency (***H***). The number inside the bar
775 represents the total number of FoV (***A***, ***B***) or trajectories (**C**, ***E-H***) analyzed from *n*=6
776 coverslips (three independent cultures). Inset: box-plots representation of the same
777 dataset. See also Figure 4-1.
778
779 **Figure 5**. Effect of AßF and AßO on the mobility of LysoTracker-labelled lysosomes
780 and their transport in mouse cortical neurons at DIC21. 24 h exposure to AßF and
781 AßO at 1 μM concentration, compared to nothing added control. ***A***, Number of
782 lysosomes detected per field-of-view of 40 x 80 μm size during 2 mins of observation.

B, Fraction of lysosomes having a directed motion. ***C***, Length of lysosome trajectories. ***D***, Examples of lysosome trajectories. Scale bar: 10 μm. ***E***-***H***, Comparison of four transport parameters: curvilinear velocity (***E***), run length (***F***), pausing time (***G***) and pausing frequency (***H***). I-J) Comparison of Lysosome size. The number inside the bar represents the total number of FoV (***A***, ***B***), trajectories (***E***-***H***) and lysosomes (***I***, ***J***) analyzed from *n*=2 coverslips (from one culture). Inset: box-plots representation of the same dataset.See also Figure 5-1, 5-2 and 5-3.

Figure 6. Intraneuronal transport of ATTO 488-labeled α-synF and R in mouse cortical neurons at DIC21. DIC20 cortical neurons were exposed to α-synF and R during 24 h, at concentration of 0.2 μM. ***A***-***B***, Examples of α-synF and R, and FND trajectories (in the presence of α-synF and R). Scale bar: 10 μm**.** ***C***, Length of α-synF, α-synR and FND trajectories. ***D***-***G***, Comparison of four transport parameters: curvilinear velocity (***D***), run length (***E***), pausing time (***F***) and pausing frequency (***G***). The number inside the bar represents the total number of trajectories analyzed from *n*=8 coverslips (four independent cultures) is indicated in each bar. Inset: box-plots representation of the same dataset.

Figure 7. Intraneuronal transport of ATTO 488-labeled AßF and AßO in mouse cortical neurons at DIC21. DIC20 cortical neurons were exposed to AßF and AßO (1 μM) during 24 h. ***A***-***B***, Examples of trajectories. Scale bar: 10 μm. ***C***, Length of AßF, AßO and FND trajectories. ***D***-***G***, Comparison of four transport parameters: curvilinear velocity (***D***), run length (***E***), pausing time (***F***) and pausing frequency (***G***). The number inside the bar represents the total number of trajectories analyzed from

806 *n*=6 coverslips (from three independent cultures) is indicated in each bar. Insets: box
807 plots representation of the same dataset. See also Figure 7-1.

808 **Figure 8.** Colocalized events between moving neurodegenerative disease-related
809 molecular species and moving lysosomes at different time points. ***A***, α-synF and α-
810 synR were incubated for 24 and 48 h, at concentration of 0.2 μM. ***B***, AßF and AßO
811 were incubated for 24 and 48 h, at concentration of 1 μM. The number inside the
812 donut plot represents the percentage of moving α-syn or Aß assemblies colocalized
813 with lysosomes (LysoTracker labelled). The table on the right panel indicates the
814 number of neurodegenerative-related molecular species trajectories colocalized with
815 lysosomes. n represents the total number of trajectories. The percentage and number
816 of trajectories in each time point were analyzed from 2 coverslips (from one culture).
817 See also Figure 8-1.

818

819 # Figures

820 ## Figure 1

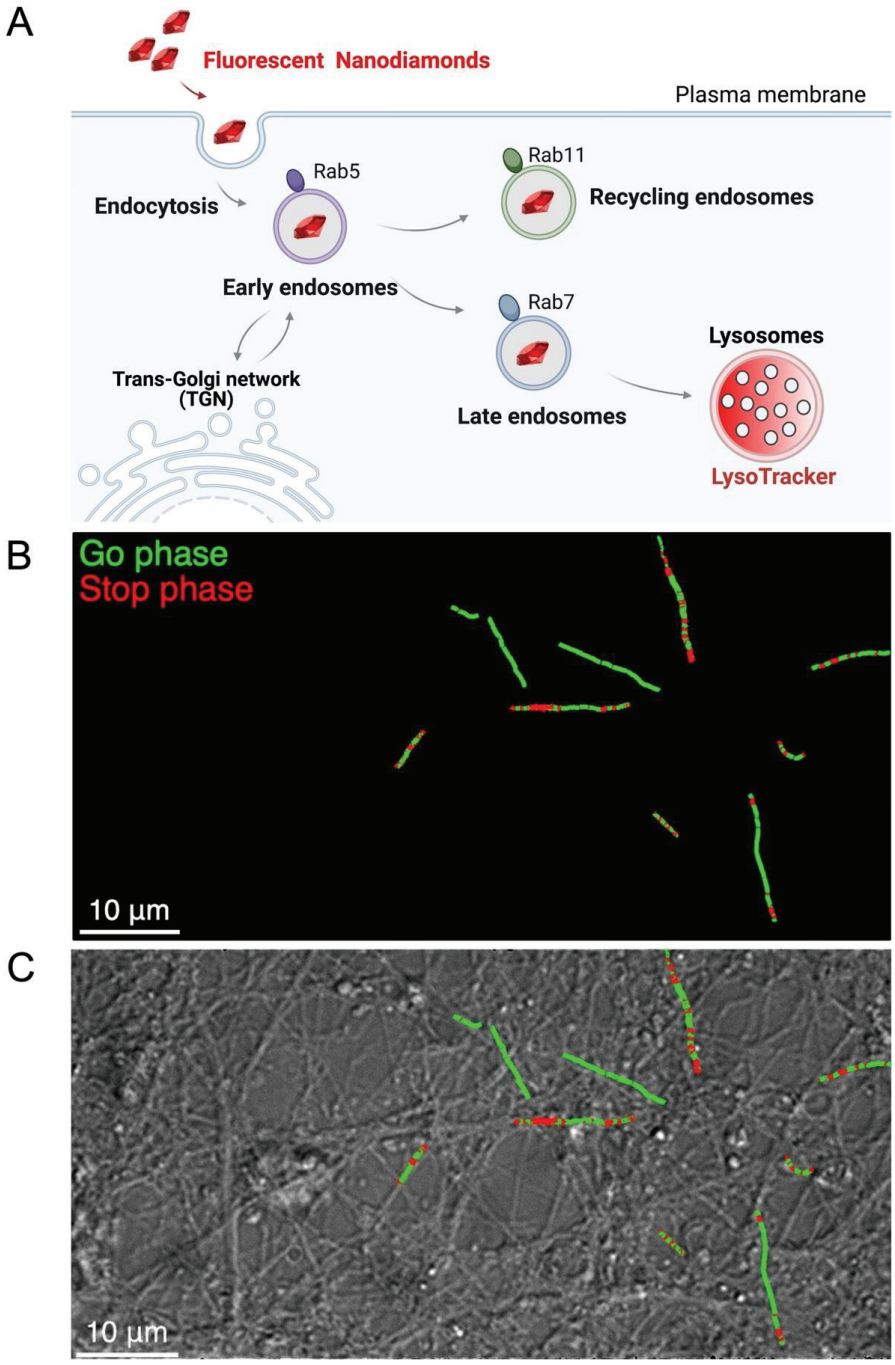

821

822

823 **Figure 2**

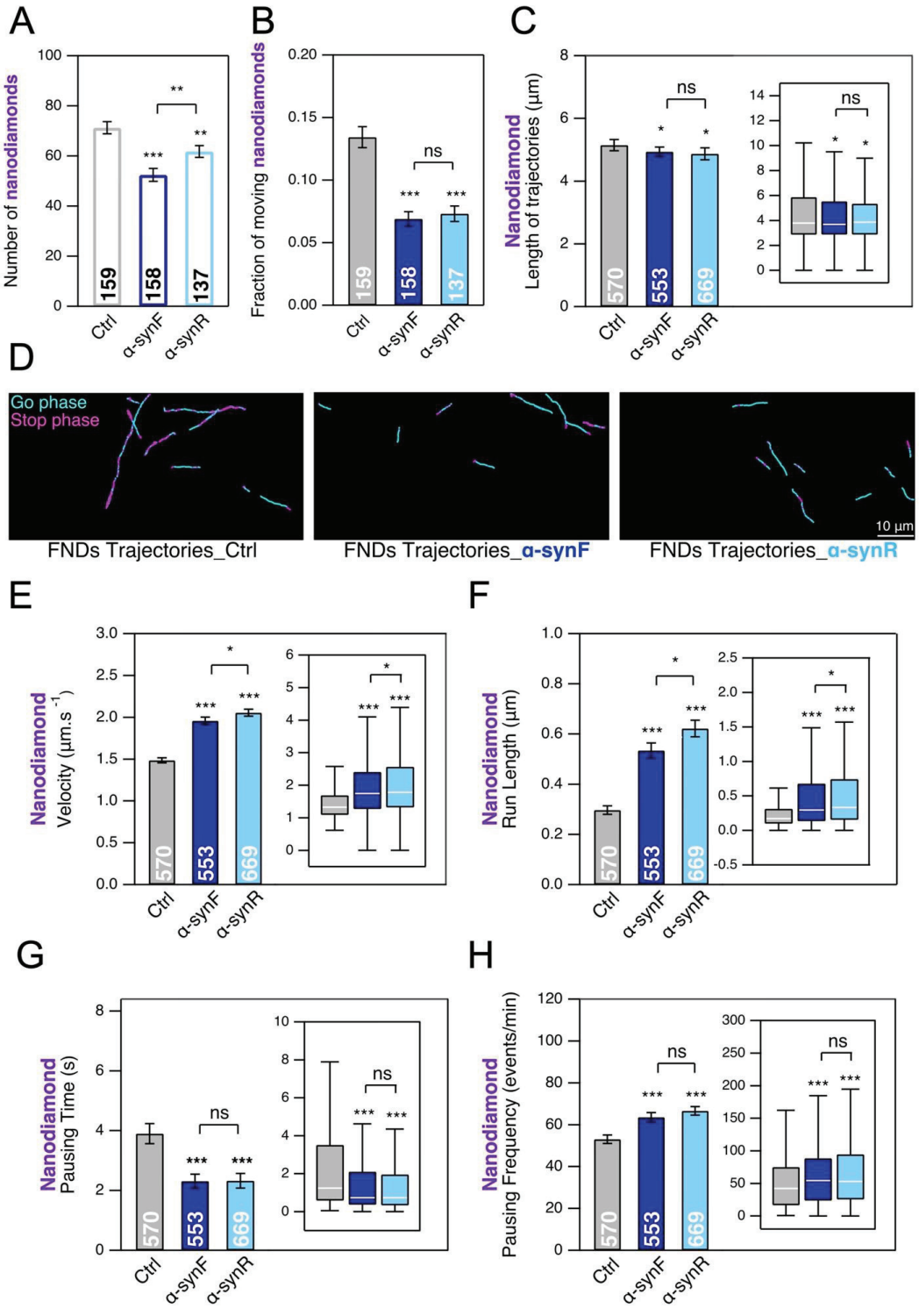

824
825

826 **Figure 3**

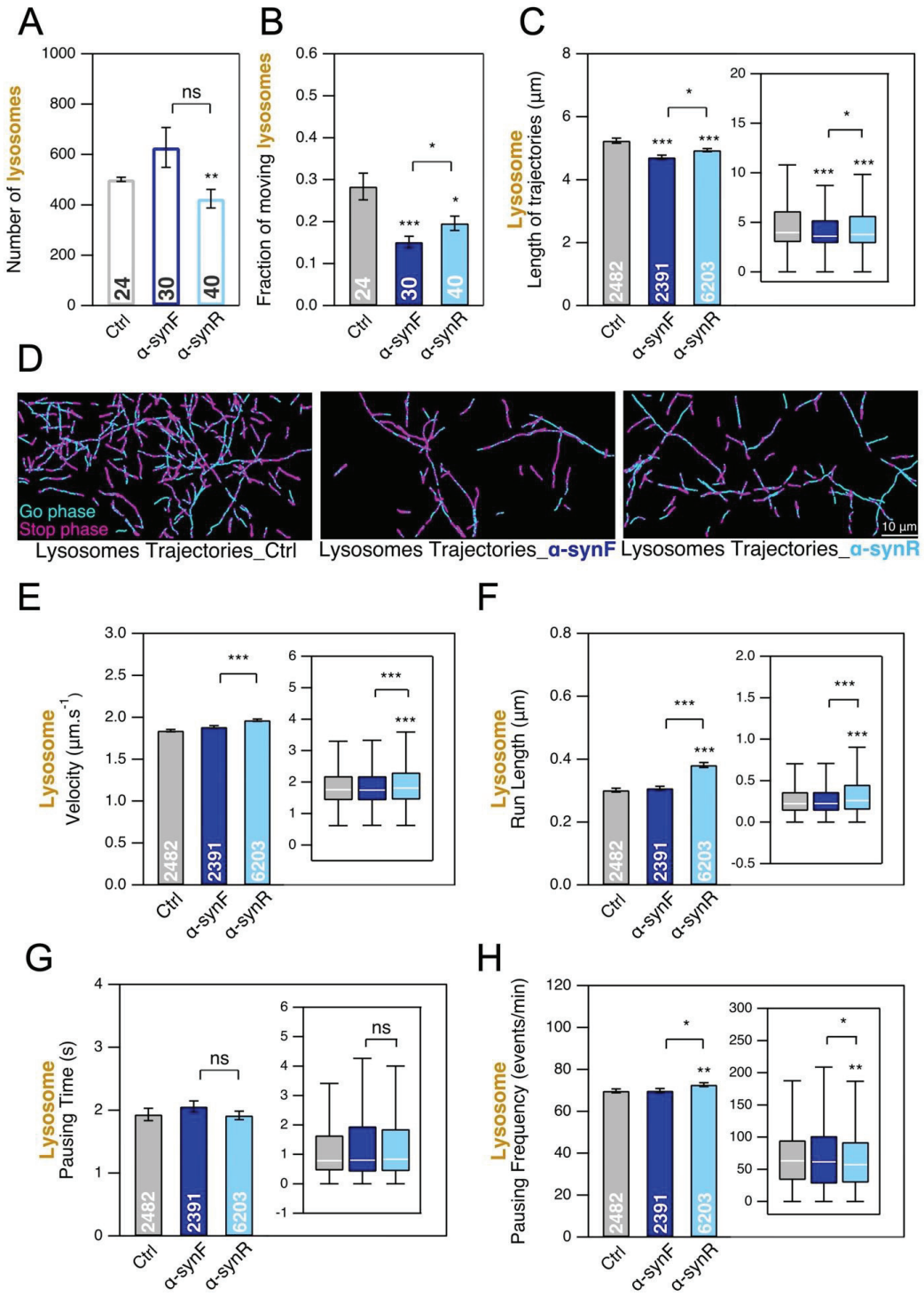

827

828

829 **Figure 4**

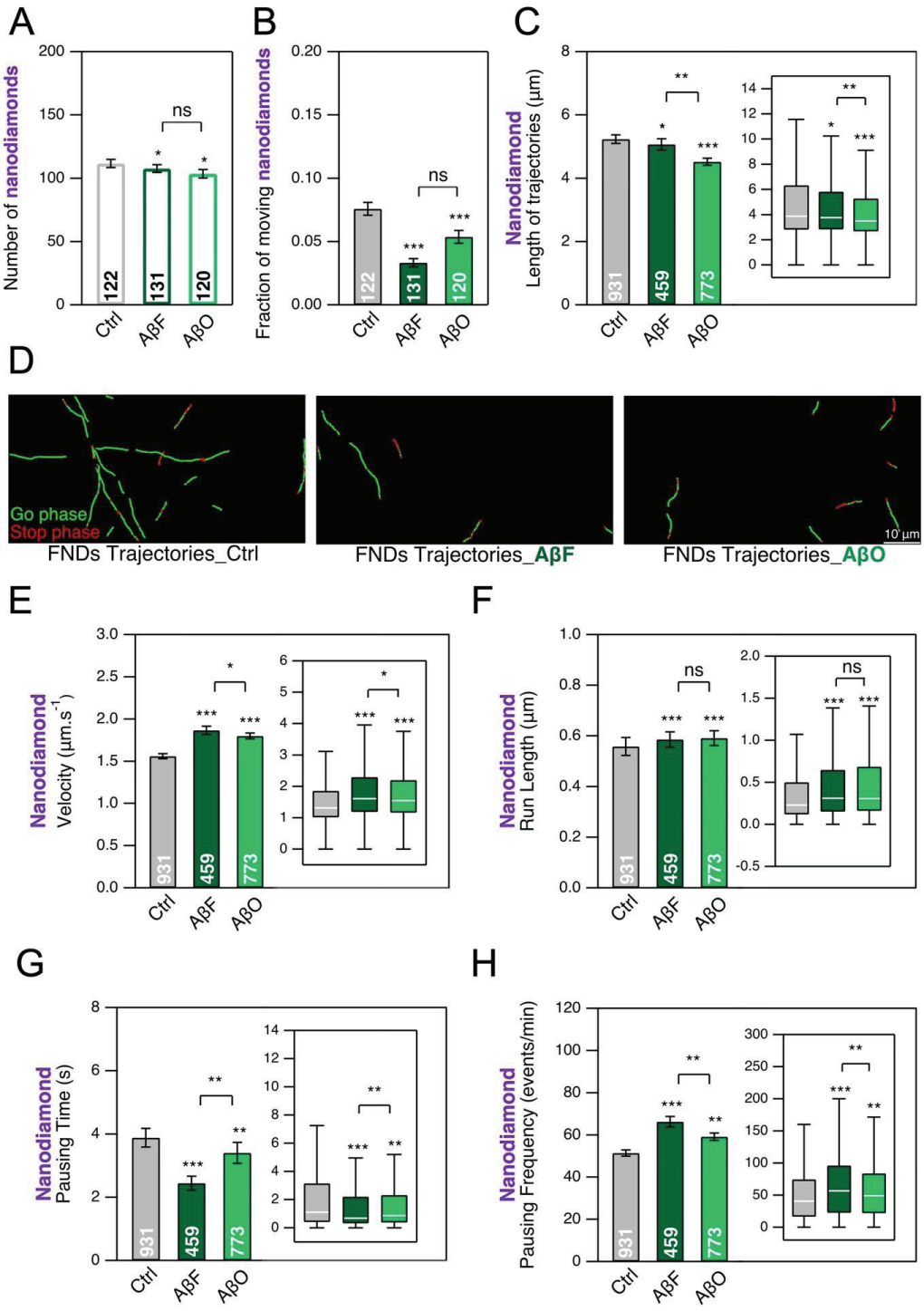

830

831

832 **Figure 5**

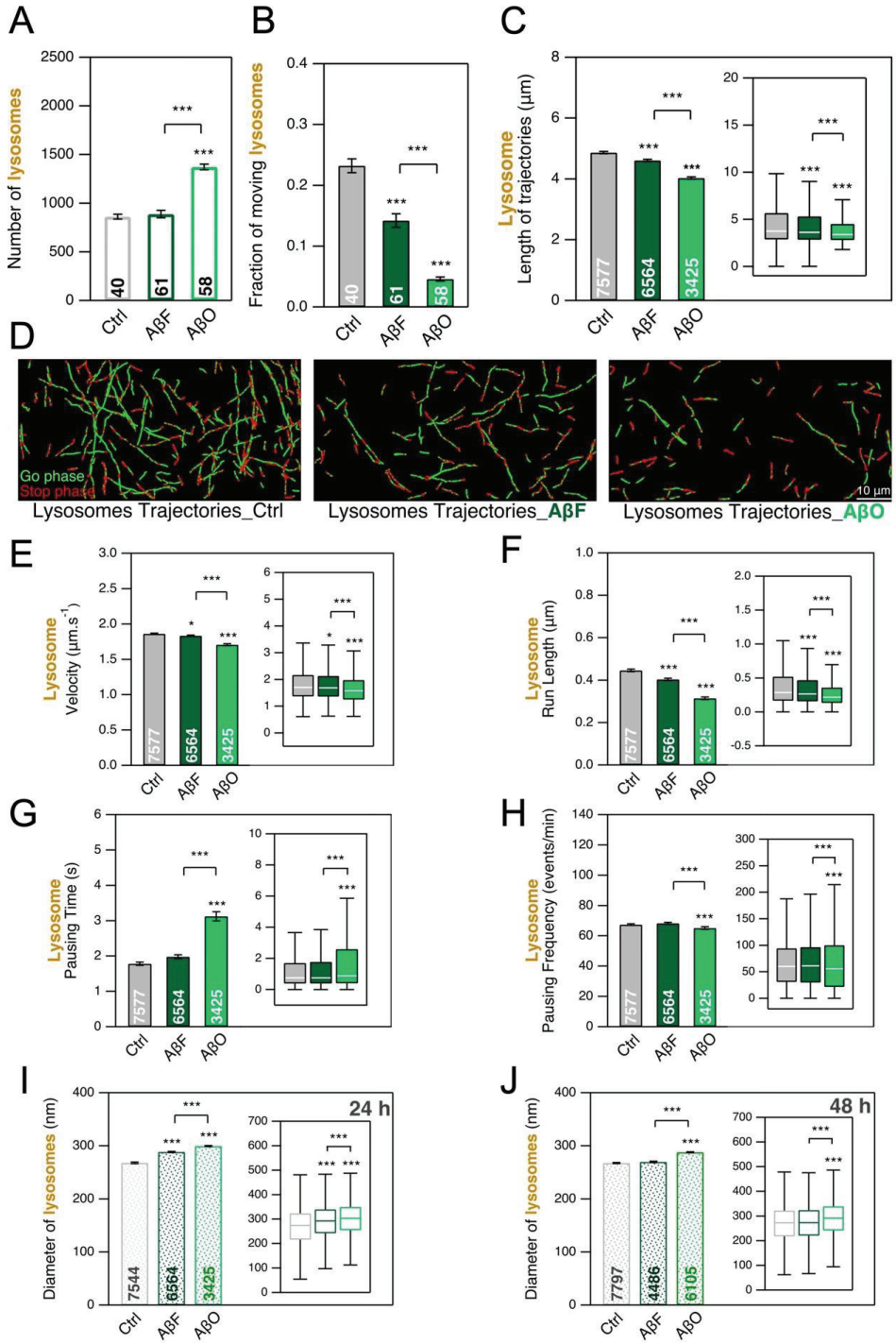

833

834

835 **Figure 6**

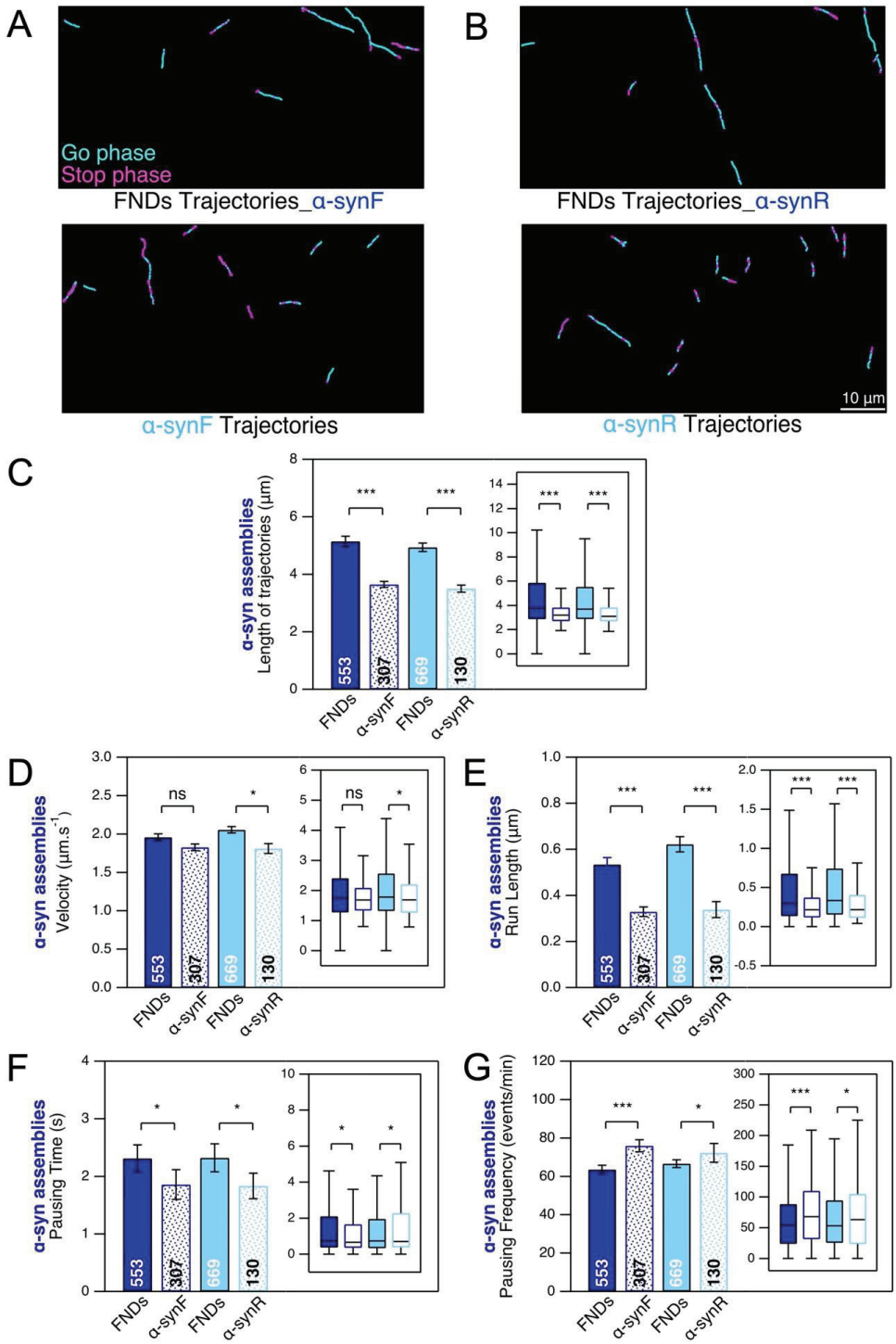

836

837

838 **Figure 7**

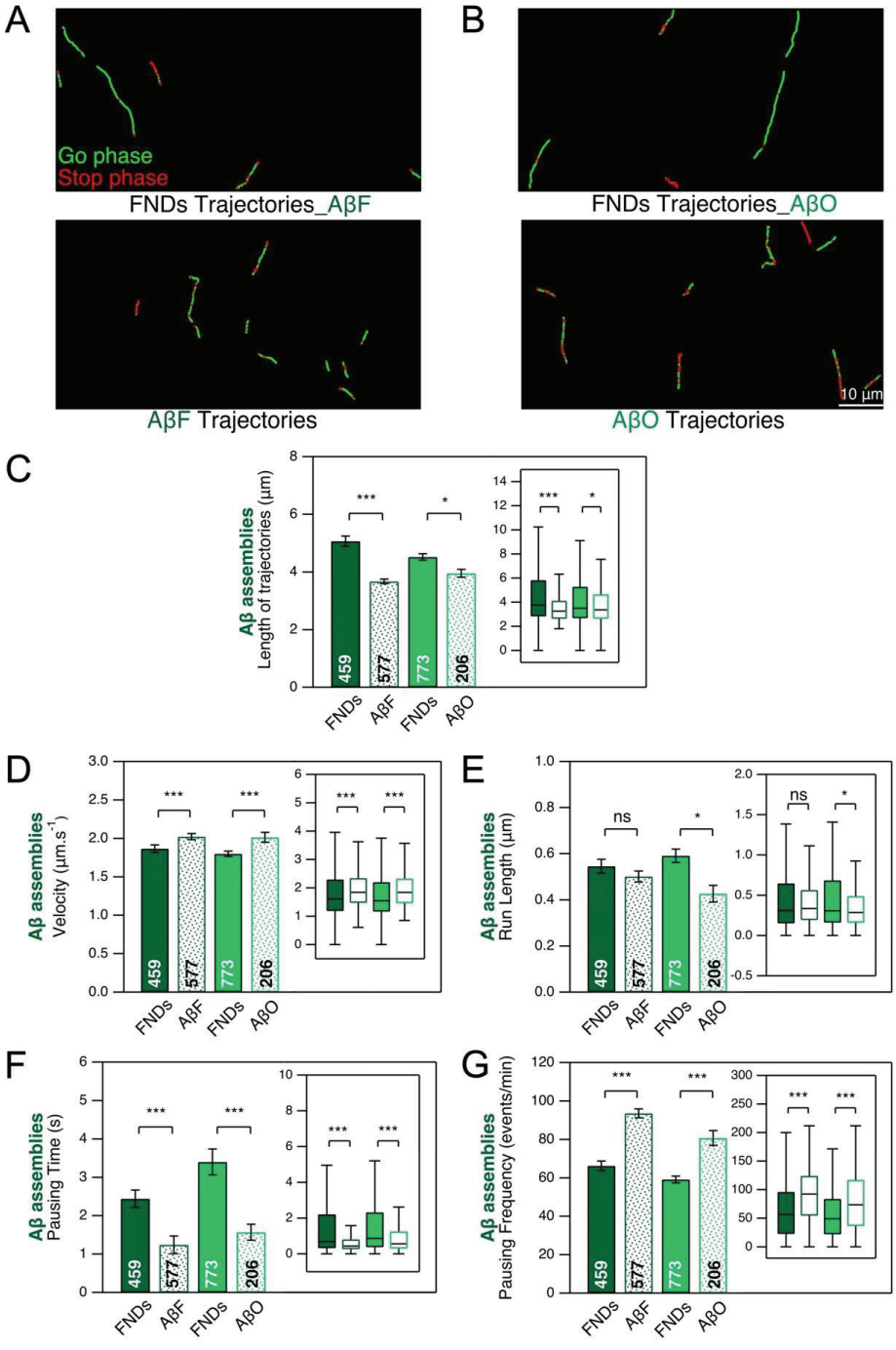

839

840

841 **Figure 8**

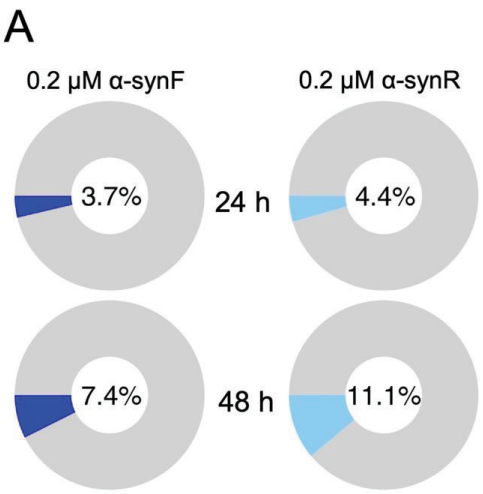

α-syn	*fibrils*	*ribbons*
24h	12 (*n*=320)	6 (*n*=135)
48h	46 (*n*=616)	19 (*n*=171)

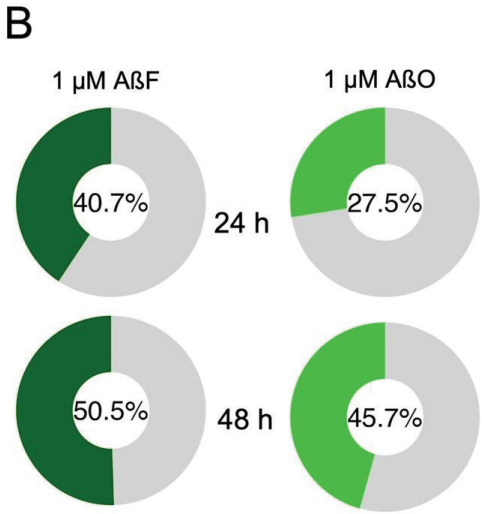

Aß	*fibrils*	*oligomers*
24h	102 (*n*=252)	22 (*n*=80)
48h	326 (*n*=646)	64 (*n*=141)

842

843

844 **Extended Figure Legends**

845

846 **Figure 2-1.** FNDs interaction with neurons and fluorescence intensity of ATTO 488-
847 labeled α-synF with and without (w/o) washing. 24 h exposure of neurons to α-synF
848 at concentration of 0.2 µM, compared to nothing added control. ***A*,** Number of FNDs
849 detected per field-of-view of 40 µm x 80 µm during 2 mins of observation for the
850 different conditions. Ctrl: no addition of α-synF; α-synF Wash: addition of α-synF
851 during 24 h and washing of the culture just before addition of FND tracers. Inset: box-
852 plots representation of the same dataset. ***B***, Fraction of FNDs-containing cargoes
853 having a directed motion. The numbers inside the bar in A and B represent the total
854 number of FOV analyzed from *n*=2 coverslips (from one culture). ***C***, Example of FND
855 trajectories in the different conditions. Scale bar: 10 µm. ***D***, Average fluorescence
856 intensity of ATTO 488-labeled α-synF evaluated for 30 µm-long branches, with or w/o
857 washing (*n*= 25 branches from 25 fields-of-view). ***E***, Examples of first frames of TIRF
858 videomicroscopy of ATTO 488-labeled α-synF decoration of DIC21 cortical neurons
859 with (top) or w/o (bottom) washing. Scale bar: 10 µm.

860

861 **Figure 2-2.** Summary of the effect of different protein assemblies on the transport
862 parameters of endosomes (***A***), LysoTracker-labeled lysosomes (***B***), and Magic Red-
863 labeled lysosomes (***C***).

864

865 **Figure 4-1.** Impact of Aβ fibrils and oligomers at the concentration of 0.2 µM on the
866 number of nanodiamonds interacting with cells (***A***), on the fraction of moving
867 nanodiamonds (***B***) and on the FND-labelled endosome transport parameters (***C-F***).

868

869 **Figure 5-1.** Lysotracker-labelled compartments size in control (***A***) and 24 h exposure
870 of Aß fibrils (***B***) and oligomers (***C***) at concentration of 1 µM. Scale bar: 2 µm.

871

872 **Figure 5-2.** Effect of α-synF on the mobility of Magic Red-labelled lysosomes and
873 their transport in mouse cortical neurons at DIC21, after 24 h exposure to α-synF at
874 concentration of 0.2 µM, compared to nothing added control. ***A***, Number of
875 lysosomes detected per field-of-view of 40 µm x 80 µm size during 2 mins of
876 observation. ***B***, Fraction of lysosomes having a directed motion. ***C***, Trajectory length.
877 ***D***, Examples of lysosome trajectories. Scale bar: 10 µm. ***E-H***, Comparison of four

878 transport parameters: **E)** curvilinear velocity (***E***), run length (***F***), pausing time (***G***) and
879 pausing frequency (***H***). ***I***, Diameter of Magic Red-labelled lysosomes. General
880 remarks: the number inside the bar represents the total number of FoV (***A***, ***B***),
881 trajectories (***E***-***I***). Inset: box-plots representations of the same datasets (***C***-***I***).
882
883 **Figure 5-3.** Effect of AßF on the mobility of Magic Red-labelled lysosomes and their
884 transport in mouse cortical neurons at DIC21 after 24 h exposure to AßF at
885 concentration of 1 µM, compared to nothing added control. ***A***, Number of lysosomes
886 detected per field-of-view of 40 µm x 80 µm size during 2 mins of observation. ***B***,
887 Fraction of lysosomes having a directed motion. ***C***, Trajectory length. ***D***, Examples of
888 lysosome trajectories. Scale bar: 10 µm. (***E***-***H***) Comparison of four transport
889 parameters: curvilinear velocity (***E***), run length (***F***), pausing time (***G***) and pausing
890 frequency (***H***). ***I***, Comparison of Magic Red-labelled lysosome size. General remarks:
891 The number inside the bar represents the total number of FoV (***A***, ***B***) and trajectories
892 (***E***-***I***) Inset: box-plots representation of the same dataset.
893
894 **Figure 7-1.** Number of AßF and AßO trajectories detected per field-of-view of 40 x 80
895 µm during 2 mins of observation. Cortical neurons were exposure to AßF and AßO
896 (1µM) during 24 h (***A***) and 48 h (***B***). The number inside the bar represents the total
897 number of FOV analyzed from *n*= 6 coverslips (from three cultures) for 24 h and *n*=2
898 coverslips (from one culture).
899
900 **Figure 8-1**. Fraction of protein assemblies, α-synF (***A***) or AßF (***B***) trajectories
901 colocalizing with Magic Red puncta trajectories, as inferred from the tables indicating
902 the number of protein assembly trajectories colocalizing with Magic Red puncta and
903 the total number of assembly trajectories in parenthesis. Data from 2 coverslips and
904 one culture in both α-synF and Aß cases.
905